

## Unraveling Radical and Oxygenate Routes in the Oxidative Dehydrogenation of Propane over Boron Nitride

Zihao Zhang, Jinshu Tian, Xiangkun Wu, Ivan Surin, Javier Pérez-Ramírez,\* Patrick Hemberger,\* and Andras Bodi\*

Cite This: *J. Am. Chem. Soc.* 2023, 145, 7910–7917

Read Online

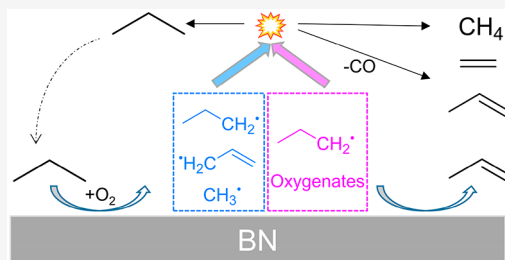
ACCESS |

Metrics &amp; More

Article Recommendations

Supporting Information

**ABSTRACT:** Oxidative dehydrogenation of propane (ODHP) is an emerging technology to meet the global propylene demand with boron nitride (BN) catalysts likely to play a pivotal role. It is widely accepted that gas-phase chemistry plays a fundamental role in the BN-catalyzed ODHP. However, the mechanism remains elusive because short-lived intermediates are difficult to capture. We detect short-lived free radicals ( $\text{CH}_3^\bullet$ ,  $\text{C}_3\text{H}_5^\bullet$ ) and reactive oxygenates,  $\text{C}_{2-4}$  ketenes and  $\text{C}_{2-3}$  enols, in ODHP over BN by *operando* synchrotron photoelectron photoion coincidence spectroscopy. In addition to a surface-catalyzed channel, we identify a gas-phase H-acceptor radical- and H-donor oxygenate-driven route, leading to olefin production. In this route, partially oxidized enols propagate into the gas phase, followed by dehydrogenation (and methylation) to form ketenes and finally yield olefins by decarbonylation. Quantum chemical calculations predict the  $>\text{BO}$  dangling site to be the source of free radicals in the process. More importantly, the easy desorption of oxygenates from the catalyst surface is key to prevent deep oxidation to  $\text{CO}_2$ .



## INTRODUCTION

Propylene ( $\text{C}_3\text{H}_6$ ) is a crucial platform chemical in the petrochemical industry for organic and polymer synthesis. It is mainly produced by petroleum-derived steam cracking and fluid catalytic cracking.<sup>1–3</sup> The annual  $\text{C}_3\text{H}_6$  production was 130 Mt in 2019 and is projected to grow to 191 Mt by 2030.<sup>4</sup> The recent shift from petroleum-derived naphtha to shale gas feedstock greatly increases the availability of ethylene ( $\text{C}_2\text{H}_4$ ) and results in a gap between the supply of  $\text{C}_3\text{H}_6$  and rising global demand.<sup>5,6</sup> To alleviate the “propylene gap”, the nonoxidative dehydrogenation of propane ( $\text{C}_3\text{H}_8$ ) was industrialized recently by Honeywell UOP (Oleflex) and ABB Lummus (Catofin).<sup>7,8</sup> However, this process suffers from (1) rapid accumulation of coke, which requires frequent catalyst regeneration, and (2) high energy need due to the endothermicity of the process.<sup>9,10</sup> Therefore, the oxidative dehydrogenation of propane (ODHP) represents a promising alternative, with an estimated energy saving of ca. 45% due to its exothermicity, as well as the prevention of coke formation in the presence of  $\text{O}_2$ .<sup>11–14</sup> Transition metal oxide catalysts, such as vanadia species ( $\text{VO}_x$ ), are able to activate C–H bonds in  $\text{C}_3\text{H}_8$ , bonding well for ODHP performance.<sup>15–18</sup> However, the partially occupied d-orbitals in transition metal oxides interact with the reactive intermediates, binding them strongly to the catalyst surface and leading to overoxidation to CO and  $\text{CO}_2$ , limiting the selectivity of the process.<sup>11,19,20</sup>

In 2016, boron nitride (BN) emerged as a unique ODHP catalyst because of its high selectivity to  $\text{C}_3\text{H}_6$  and the prevention of  $\text{CO}_x$ , especially  $\text{CO}_2$ , formation.<sup>21</sup> Modified

BN<sup>22,23</sup> and further boron-containing catalyst candidates, e.g., boron oxides ( $\text{BO}_x$ ),<sup>24–27</sup> were widely studied to identify the active site. The similar reaction kinetics over BN and  $\text{BO}_x$  were rationalized by surface oxygen functionalization on BN, generating  $\text{BO}_x$  sites as the effective active site in ODHP.<sup>28,29</sup> The conversion was found to increase with higher dilution over boron-based catalysts, which was one of the peculiar kinetic features implying a gas-phase  $\text{C}_3\text{H}_6$  formation route.<sup>30</sup> Based on computational results and kinetic measurements, distinct surface-confined and gas-phase mechanisms were, thus, proposed over boron-based catalysts for ODHP.<sup>31–33</sup> So far, the only experimental evidence for the existence of a gas-phase route has been the observation of the methyl radical.<sup>34</sup> The gas-phase reaction mechanism and the possibility of free radical involvement beyond the methyl radical remain unknown, which makes it challenging to rationally optimize catalysts for the practical application of ODHP.

In this contribution, we shed light on the intermediates and products evolving in real time in ODHP over BN by *operando* synchrotron photoelectron photoion coincidence (PEPICO) spectroscopy. *Operando* PEPICO detects short-lived reactive

Received: December 9, 2022

Published: March 3, 2023



intermediates, e.g., radicals, ketenes, and enols, desorbed from the catalyst surface<sup>35,36</sup> and, thus, provides direct experimental evidence to understand the ODHP reaction network over BN. A silica-supported vanadia catalyst ( $\text{VO}_x/\text{SiO}_2$ ) was also studied for direct comparison with the catalytic mechanism over BN. Temperature-dependent ODHP experiments in a tubular continuous-flow reactor coupled to the PEPICO endstation also provide temperature profiles of stable species and reactive intermediates. Surface-confined density functional theory (DFT) calculations on boron active sites and gas-phase G4 calculations reveal the formation mechanism of short-lived radical intermediates detected by *operando* PEPICO spectroscopy. A reaction mechanism for boron-catalyzed ODHP is proposed, encompassing coupled surface-confined and gas-phase reaction steps.

## RESULTS AND DISCUSSION

**ODHP as a Function of Temperature over BN and  $\text{VO}_x/\text{SiO}_2$ .** The temperature-dependent ODHP performance over commercial BN and homemade  $\text{VO}_x/\text{SiO}_2$  catalysts is compared in Figure 1. Over the BN catalyst, the main products

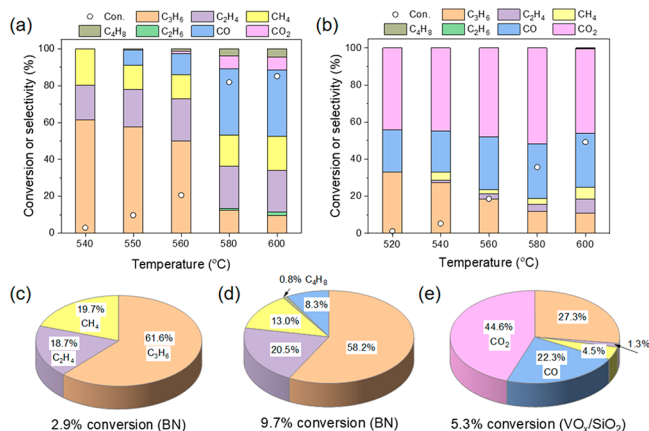


**Figure 1.** Influence of reaction temperature on catalytic ODHP performance over (a) BN and (b)  $\text{VO}_x/\text{SiO}_2$ ; the product selectivity over BN at  $\text{C}_3\text{H}_8$  conversions of (c) 2.9% and (d) 9.7%, as well as over  $\text{VO}_x/\text{SiO}_2$  at  $\text{C}_3\text{H}_8$  conversion of (e) 5.3%. Reaction conditions: 20 mg catalyst, feed: 10%  $\text{C}_3\text{H}_8$  and 20%  $\text{O}_2$  balanced in Ar; 66 mL/min total flow rate.

are propene, ethene, and methane at temperatures below 560 °C with the propane conversion lower than 21% (Figure 1a). Small amounts of CO and butene isomers ( $\text{C}_4\text{H}_8$ ) are also found at 550–560 °C. When increasing the temperature so that the  $\text{C}_3\text{H}_8$  conversion rises to above 80%, the selectivity to  $\text{C}_3\text{H}_6$  decreases with increased formation of  $\text{CO}$ ,  $\text{CO}_2$ , and  $\text{C}_4\text{H}_8$ . In contrast, the main products over a  $\text{VO}_x/\text{SiO}_2$  catalyst are  $\text{C}_3\text{H}_6$  and  $\text{CO}_x$  (Figure 1b), the latter being predominant at high  $\text{C}_3\text{H}_8$  conversion. This indicates that overoxidation can be curtailed using the BN catalyst, especially at low  $\text{C}_3\text{H}_8$  conversion. As a result, the total selectivity to hydrocarbons ( $\text{C}_3\text{H}_6$ ,  $\text{C}_2\text{H}_4$ , and  $\text{CH}_4$ ) over BN is significantly higher than over  $\text{VO}_x/\text{SiO}_2$  at a comparable  $\text{C}_3\text{H}_8$  conversion. For example, the selectivities to  $\text{C}_3\text{H}_6$ ,  $\text{C}_2\text{H}_4$ , and  $\text{CH}_4$  are 61.6%, 18.7%, and 19.7%, respectively, at a  $\text{C}_3\text{H}_8$  conversion of 2.9% over a BN catalyst (Figure 1c), which corresponds to essentially full selectivity to hydrocarbons. Increasing the  $\text{C}_3\text{H}_8$  conversion to 9.7%, the selectivity to  $\text{C}_3\text{H}_6$ ,  $\text{C}_2\text{H}_4$ , and  $\text{CH}_4$  is still ca. 92%, while 0.8%  $\text{C}_4\text{H}_8$  and 8.3%  $\text{CO}$  are also

formed over BN (Figure 1d). This can be compared with only 27.3% selectivity to  $\text{C}_3\text{H}_6$  with dominant production of  $\text{CO}$  and  $\text{CO}_2$  already at 5.3% conversion over  $\text{VO}_x/\text{SiO}_2$  (Figure 1e).

The selectivity to  $\text{CO}_2$  is always low over BN, and  $\text{CO}$  is the main overoxidized product at high temperatures, as opposed to the  $\text{VO}_x/\text{SiO}_2$  catalyst, where  $\text{CO}_2$  dominates. Another difference between the BN and  $\text{VO}_x/\text{SiO}_2$  catalysts is that small amounts of  $\text{C}_4\text{H}_8$  isomers are only observed over BN. The product distributions over BN and  $\text{VO}_x/\text{SiO}_2$  catalysts (Figure 1) are consistent with previous results.<sup>34,37</sup> However, the origin of the high selectivity to  $\text{C}_3\text{H}_6/\text{C}_2\text{H}_4$  and the inhibition of overoxidation to  $\text{CO}_x$  (especially to  $\text{CO}_2$ ) over BN have remained unclear so far and are the subject of this study.

**Operando PEPICO Spectroscopy.** Operando synchrotron PEPICO spectroscopy<sup>38,39</sup> was utilized to detect stable products and elusive ODHP intermediates over BN and  $\text{VO}_x/\text{SiO}_2$  catalysts. The PEPICO setup is described in Figure S1. In brief, a gas mixture of  $\text{C}_3\text{H}_8$ ,  $\text{O}_2$ , and Ar is fed into the preheated catalyst bed, and the continuous gas flow, with reactants, intermediates, and final products, expands from the reactor into high vacuum, forming a molecular beam. Molecular beam sampling freezes out the chemistry and suppresses quenching. The molecular beam travels through the skimmer and crosses the monochromatic vacuum ultraviolet beam in the ionization region. Soft photoionization yields photoelectrons and -ions, which are detected in delayed coincidence. Ion mass analysis yields photoionization mass spectra and, combined with electron kinetic energy analysis, allows us to plot photoion mass-selected threshold photoelectron spectra (ms-TPES) to identify the spectral carrier(s) of individual  $m/z$  peaks isomer-selectively.<sup>40,41</sup> Mass spectra and ms-TPES are first compared at 600 °C based on a temperature-programmed surface reaction (TPSR) of adsorbed propane ( $\text{C}_3\text{H}_8$ ) on BN from 500 to 700 °C (Figure S2). During ODHP operation, the  $m/z$  42 peak dominates over both BN and  $\text{VO}_x/\text{SiO}_2$ , while the  $\text{C}_2\text{H}_4$  ( $m/z$  28) and  $\text{CH}_4$  ( $m/z$  16) signals are much more intense over BN than over  $\text{VO}_x/\text{SiO}_2$  (Figure 2a,b), consistent with the product distribution seen in Figure 1. A blank experiment without catalyst shows negligible product formation under the same conditions (Figure S3).

Moreover, small  $m/z$  56 and 58 peaks are only visible over BN (Figure 2a). Based on the comparison of the  $m/z$  42 ms-TPES with the propene and ethenone ketene reference spectra (Figure 2d), this peak can be assigned exclusively to  $\text{C}_3\text{H}_6$  over  $\text{VO}_x/\text{SiO}_2$  and to a mixture of  $\text{C}_3\text{H}_6$  and  $\text{C}_2\text{H}_2\text{O}$  over BN. The ms-TPES of  $m/z$  56 (Figure 2f) is assigned to a mixture of methylketene ( $\text{C}_3\text{H}_4\text{O}$ ,  $\text{CH}_3\text{—CH=C=O}$ ), 2-propenal ( $\text{C}_3\text{H}_4\text{O}$ ,  $\text{CH}_2\text{=CH—CH=O}$ ), and  $\text{C}_4\text{H}_8$  (1-, 2-butene, and isobutene) over BN, based on reference and Franck–Condon simulated spectra. In contrast, only  $\text{C}_4\text{H}_8$  is observed in Figure 1a as a final product. To the best of our knowledge, this is the first time that oxygenated species such as ketenes are observed as ODHP intermediates, likely because ketene and methylketene are unstable and evade detection by GC/MS even if present in the effluent.<sup>42,43</sup> This illustrates the advantage of *operando* PEPICO in detecting elusive intermediates to provide mechanistic insights into catalytic mechanisms.<sup>40</sup> The  $m/z$  58 peak can be ascribed to propen-*m*-ol isomers ( $m = 1, 2, \text{ or } 3$ ,  $\text{C}_3\text{H}_6\text{O}$ ) and propionaldehyde (Figures 2g and S4c), also newly observed in ODHP. Acetaldehyde and its

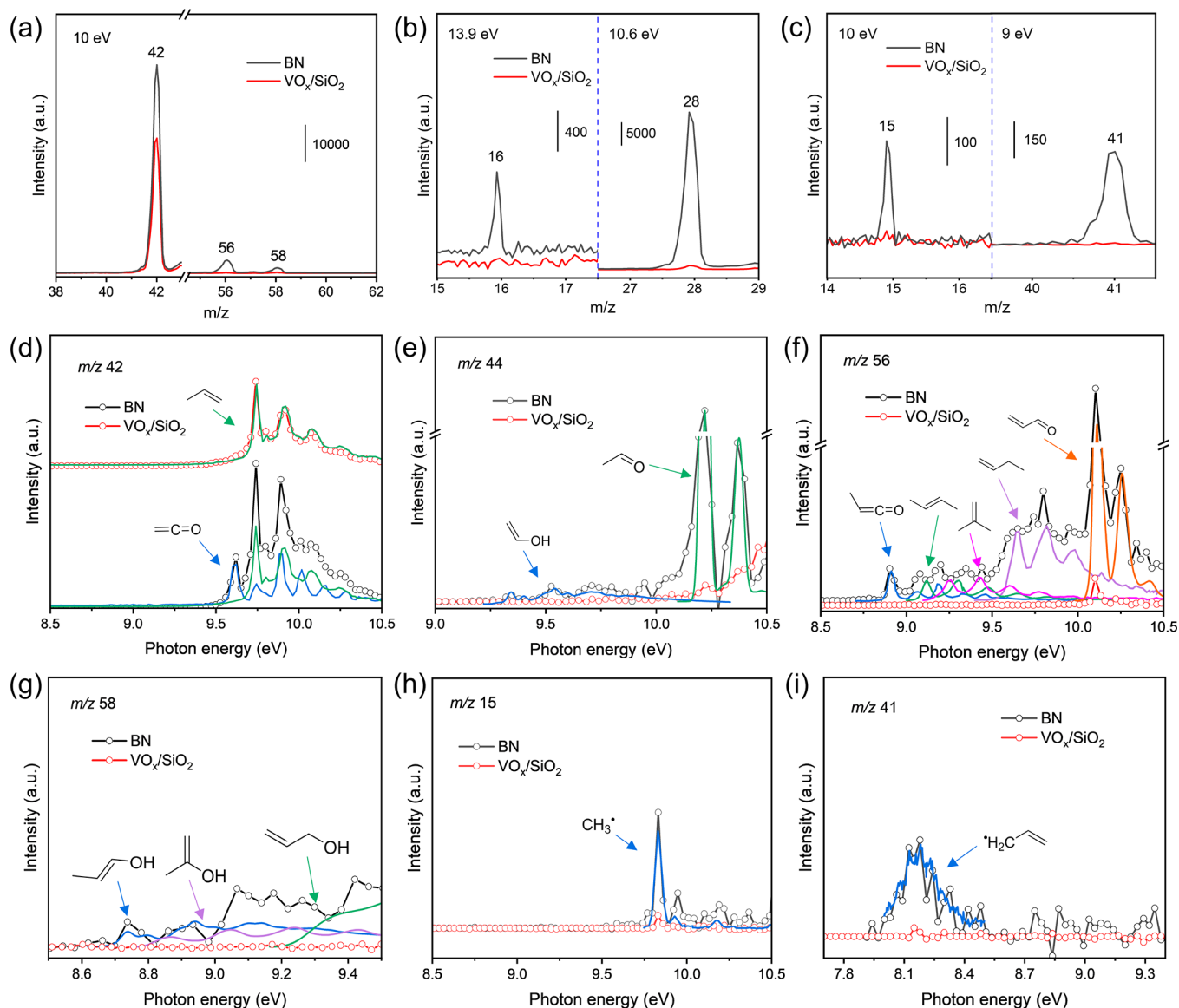


**Figure 2.** (a–c) ODHP photoionization mass spectra over BN and VO<sub>x</sub>/SiO<sub>2</sub> at 600 °C at different photon energies; ms-TPES of (d) *m/z* 42, (e) *m/z* 44, (f) *m/z* 56, (g) *m/z* 58, (h) *m/z* 15, and (i) *m/z* 41 over BN and VO<sub>x</sub>/SiO<sub>2</sub> at 600 °C; reaction conditions: 10 mg of catalyst, gas feed: 10% C<sub>3</sub>H<sub>8</sub> and 20% O<sub>2</sub> balanced in Ar; 10 mL/min total flow rate, 0.3 bar pressure; reference spectra are marked by arrows, see [Table S1](#) for details.

high-energy tautomer, ethenol (vinyl alcohol,  $\text{C}_2\text{H}_4\text{O}$ ,  $\text{CH}_2=\text{CH}-\text{OH}$ ), are detected over BN at  $m/z$  44 (Figures 2e and S5). In addition to propionaldehyde and acetaldehyde, formaldehyde ( $\text{HCHO}$ ) is also detected by its ms-TPES at  $m/z$  30 (Figure S4b). The oxygenates ( $\text{C}_{1-3}$  aldehydes,  $\text{C}_{2-3}$  ketenes, and  $\text{C}_{2-3}$  enols) found over BN represent minor peaks compared to  $\text{C}_3\text{H}_6$ ,  $\text{C}_2\text{H}_4$ , and  $\text{CH}_4$ . However, the desorption of these intermediates from the catalyst surface, as implied by their detection, is crucial in preventing overoxidation (*vide infra*). Finally, the ion peaks at  $m/z$  15 and  $m/z$  41 detected over BN (Figure 2c) can be unambiguously assigned to methyl ( $\text{CH}_3^\bullet$ ) and allyl ( $\text{C}_3\text{H}_5^\bullet$ ) radicals, respectively, based on the corresponding ms-TPES (Figure 2h and i).

Motivated by the observation of oxygenates (aldehydes, ketenes, and enols) and radicals over BN, we further investigated the temperature-dependent product distribution over BN from 550 to 700 °C. The corresponding photoionization mass spectra are shown in [Figure S6](#), while the

integrated signals are presented in Figure 3. With increasing temperature, the  $\text{CH}_3^\bullet$  signal increases together with that of  $\text{CH}_4$ , indicating that methane is likely formed by gas-phase H addition to  $\text{CH}_3^\bullet$  (see below). Since  $\text{CH}_3^\bullet$  is formed from  $\text{C}_3\text{H}_8$ , the observed  $\text{C}_2\text{H}_4$  from the counter fragment  $\text{C}_2\text{H}_5$  comes as no surprise. The  $\text{C}_3\text{H}_5^\bullet$  signal appears at 600 °C (Figure S7) and continues to increase with temperature, suggesting increasing  $\text{C}_3\text{H}_6$  decomposition at elevated temperatures. The rising  $\text{C}_3\text{H}_8$  conversion and  $\text{C}_3\text{H}_6$  activation affect the final  $\text{C}_3\text{H}_6$  signal in opposite ways and result in constant propene abundance when the temperature is increased further from 650 to 700 °C (Figure 3). Ethenol, methylketene, and propen-*m*-ol signals all increase from 550 to 650 °C, but become stable or even decrease from 650 to 700 °C (Figure 3), implying that they may also be converted further to other products. The  $m/z$  56 signal taken at a photon energy of 9.5 eV, which can be assigned primarily to  $\text{C}_4\text{H}_8$  and, to a lesser degree, methylketene (Figures S8 and S9), also increases

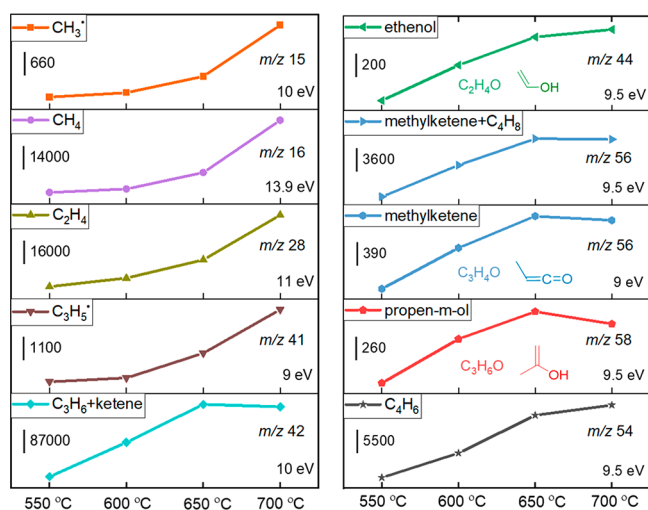


**Figure 3.** Photoionization mass spectrum peak integrals as a function of temperature in ODHP over BN; reaction conditions are the same as in Figure 2.

from 550 to 650 °C and finally becomes relatively stable. The simultaneous increase of the  $C_4H_8$  signal together with  $CH_3^*$  and  $C_3H_5^*$  from 550 to 650 °C suggests a possible gas-phase  $CH_3^* + C_3H_5^*$  reaction to yield  $C_4H_8$ . The relatively stable  $m/z$  56 signal between 650 and 700 °C is due to the simultaneous consumption of  $C_4H_8$  by dehydrogenation, yielding  $C_4H_6$  ( $m/z$  54, Figure 3).  $CH_3^*$  is produced by desorption from the catalyst surface after propane activation, because  $C_3H_8$  cracking is not observed in the blank experiment

(Figure S3). It is worth noting that  $C_2$  radicals, such as  $C_2H_5^*$ , have not been observed. We consider the role of oxygenates in the ODHP mechanism and compare it with that in combustion. Notably, typical combustion temperatures are significantly higher than the ODHP reaction temperatures of 550–600 °C. However, analogous reactions are likely to occur on ODHP catalytically, since the catalyst provides a dehydrogenation active site.<sup>44</sup> Vinyl alcohol ( $CH_2=CH-OH$ ) is less stable than its tautomer acetaldehyde<sup>45</sup> by ca. 42 kJ mol<sup>-1</sup> and yet plays a role in the partial oxidation of hydrocarbons and alcohols.<sup>46</sup> The detection of  $C_{2-3}$  enols in this work implies a possible low-temperature surface-mediated enol formation side reaction in BN-catalyzed ODHP. In contrast to  $VO_x/SiO_2$ , full oxidation to  $CO_2$  is inhibited over BN, which is explained by only weakly surface-bound partially oxidized intermediates, which readily desorb into the gas phase and are detected. The observation of ketenes has mechanistic ramifications, as well. The presence of ethylketene ( $CH_3CH_2-CH=C=O$ ) is evidenced by the  $m/z$  70 ms-TPES (Figure S10) over BN. Ketenes have been widely reported as the key intermediates for olefin formation,<sup>3,35,47,48</sup> which indicates an oxygenate-driven route in BN-catalyzed ODHP and will be addressed computationally in the following section.

**Computational Insights.** Quantum chemical calculations were carried out for both surface-catalyzed and gas-phase reactions to reveal the origin of the reactive radicals and oxygenates detected over BN by *operando* PEPICO. Analogous theoretical calculations on ODHP over  $VO_x$ -based catalysts have been carried out previously and, in light of propane overoxidation over  $VO_x$ , are not discussed here further.<sup>49–51</sup> Although a crystalline  $B_2O_3$  (101) surface was used to simplify

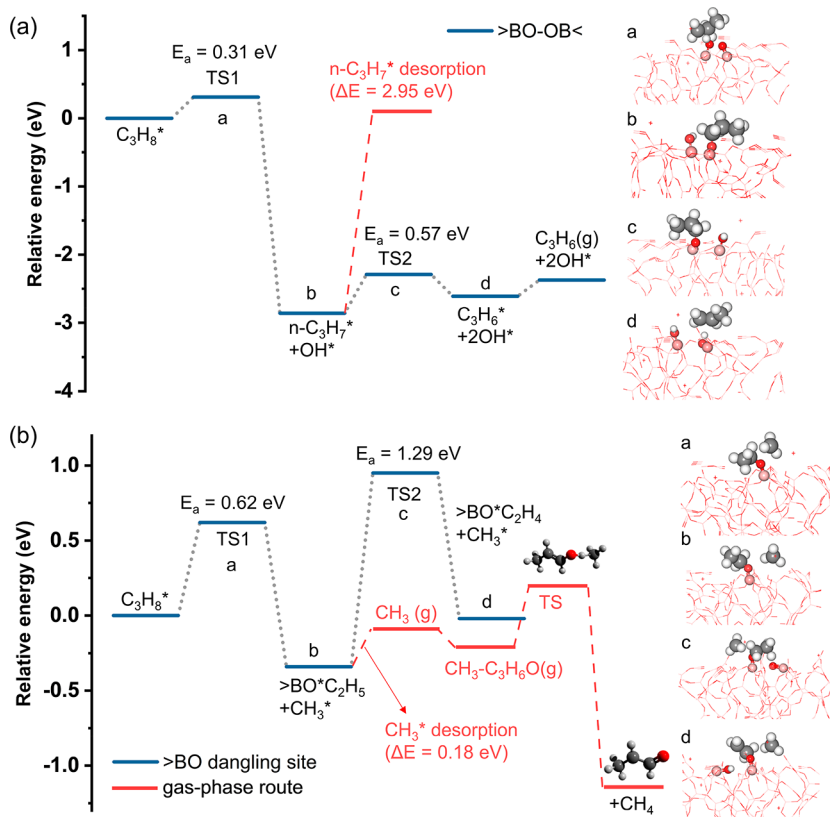


**Figure 4.** DFT-calculated energy profile for (a) C–H cleavage over the  $>BO-OB<$  site and (b) C–C cleavage over the  $>BO$  dangling site on the disordered  $B_2O_3$  (101) surface. The corresponding minima and transition states are shown on the right.



the BN active surface, it is accepted that the active catalyst surface corresponds more closely to amorphous boron oxide in ODHP.<sup>34</sup> To simulate the real catalyst surface, *ab initio* molecular dynamics (AIMD) simulations were first carried out for the  $\text{B}_2\text{O}_3$  (101) surface at the high temperatures of 1500–2000 K to achieve a disordered  $\text{BO}_x$  surface within the tractable time window of 2–4 ps (Figure S11).  $\text{O}_2$  chemisorption on  $\text{BO}_x$  forms peroxy-like  $>\text{BO}-\text{OB}<$  species preferentially, which is regarded as the main site for  $\text{C}_3\text{H}_8$  activation.<sup>28,31</sup>  $\text{O}_2$  chemisorption is modeled on the amorphous  $\text{BO}_x$  surface, and the adsorption configurations of  $\text{C}_3\text{H}_8$  on the  $>\text{BO}-\text{OB}<$  site are optimized (Figure S12). After C–H cleavage at the  $>\text{BO}-\text{OB}<$  site (Figure 4a),  $\text{C}_3\text{H}_8^*$  will transform into coadsorbed  $>\text{BO}-n\text{-C}_3\text{H}_7^*$  and  $>\text{BO}-\text{H}^*$  over a barrier of 0.31 eV (\* represents adsorbed species). The formed  $n\text{-C}_3\text{H}_7^*$  is strongly bound to the surface with nearly 3 eV desorption energy and will further dehydrogenate to yield  $\text{C}_3\text{H}_6^*$  over a barrier of only 0.57 eV. Alternatively, C–C cleavage in  $\text{C}_3\text{H}_8$  on  $>\text{BO}-\text{OB}<$  can also occur (Figure S13), but the cracked  $\text{CH}_3^*$  and  $\text{C}_2\text{H}_5^*$  radicals are also strongly bound to the surface at desorption energies of 3.69 and 3.48 eV, respectively. This is much higher than the alternative  $\text{C}_2\text{H}_4$  formation energy of 1.01 eV (Figure S14), which suggests that free radicals are not desorbed from the  $>\text{BO}-\text{OB}<$  site.

AIMD simulations of the  $\text{BO}_x$  surface also yielded a  $>\text{BO}$  dangling site occurring at 1000 K (Figure S15). This site was also proposed to be active in boron-catalyzed ODHP.<sup>31</sup> The C–C bond can be cleaved on the  $>\text{BO}$  dangling site (Figures 4b and S16). Here,  $\text{C}_3\text{H}_8^*$  transforms into either  $>\text{BO}-\text{C}_2\text{H}_5^*/\text{CH}_3^*$  or  $>\text{BO}-\text{CH}_3^*/\text{C}_2\text{H}_5^*$ . The desorption energy of  $\text{CH}_3^*$  is only 0.18 eV from the former. For  $>\text{BO}-\text{CH}_3^*/\text{C}_2\text{H}_5^*$ , calculations predict prompt  $\text{C}_2\text{H}_5^*$  dehydrogenation to  $\text{C}_2\text{H}_4^*$  (Figure S17), implying that  $\text{C}_2\text{H}_5^*$  is unlikely to desorb into the gas phase. Moreover,  $\text{C}_3\text{H}_6$  can also be activated on the  $>\text{BO}$  dangling site, readily forming gas-phase  $\text{C}_3\text{H}_5^*$  with a desorption energy of 0.33 eV (Figure S18). These results identify the  $>\text{BO}$  dangling site as the source for the experimentally observed  $\text{CH}_3^*$  and  $\text{C}_3\text{H}_5^*$  radicals. In addition to the C–C cleavage route on the  $>\text{BO}$  dangling site, we also found a comparable C–H cleavage barrier toward  $n\text{-C}_3\text{H}_7^*$  and  $i\text{-C}_3\text{H}_7^*$  (Figure S19). The adsorbed  $i\text{-C}_3\text{H}_7^*$  intermediate will spontaneously transform into  $\text{C}_3\text{H}_6$  by terminal H abstraction (Figure S20). In contrast,  $n\text{-C}_3\text{H}_7^*$  may either transform into  $\text{C}_3\text{H}_6$  over a barrier of 0.17 eV or propagate into the gas phase with a desorption energy of only 0.39 eV (Figure S21). Despite surface-catalyzed  $n\text{-C}_3\text{H}_7^*$  to  $\text{C}_3\text{H}_6$  conversion having a lower energy barrier,  $n\text{-C}_3\text{H}_7^*$  desorption may effectively compete, especially at high temperatures. The propyl radical intermediate was, however, not detected experimentally in the gas phase, in contrast to  $\text{CH}_3^*$  and  $\text{C}_3\text{H}_5^*$ . We first have to consider gas-phase radical chemistry to conclude whether this indicates nondesorption or a short gaseous lifetime of  $n\text{-C}_3\text{H}_7$ .

In addition to radicals, gas-phase reactive oxygenates are also detected by *operando* PEPICO. As guided by previous gas-phase mechanistic insights on, for example, the role of enols in combustion,<sup>44</sup> we applied the G4 composite method to address possible gas-phase reaction pathways. The formation of enols and ketenes may proceed similarly to a combustion chemistry pathway. Enols, for instance, are likely produced via partial hydrocarbon oxidation on the catalyst surface in ODHP, followed by desorption into the gas phase. In the gas phase, the allyl +  $\text{O}_2$  reaction affords formaldehyde

(observed in Figure S4) and the  $\text{H}_2\text{C}-\text{C}(=\text{O})\text{H}$  radical, in an exothermic reaction (−2.75 eV) after an entrance barrier of 0.55 eV,<sup>52</sup> which is likely reduced in the presence of BN. The  $\text{H}_2\text{C}-\text{C}(=\text{O})\text{H}$  radical can either be dehydrogenated to yield ketene or hydrogenated to vinyl alcohol or acetaldehyde ( $m/z$  44, Figures S5, S8), which were all observed in this study. On the one hand, we found computationally that  $\text{C}_{2-3}$  enols ( $\text{C}_2\text{H}_4\text{O}$ ,  $\text{C}_3\text{H}_6\text{O}$ ) can be converted to  $\text{C}_{2-3}$  ketenes ( $\text{C}_2\text{H}_2\text{O}$ ,  $\text{C}_3\text{H}_4\text{O}$ ) via dehydrogenation by, for example, a  $\text{CH}_3^*$  radical over a low energy barrier of 0.46 eV for  $\text{C}_2\text{H}_4\text{O}$  and 0.40 eV for  $\text{C}_3\text{H}_6\text{O}$  (Figure S22). This H abstraction step of propen-1-ol by  $\text{CH}_3^*$  after  $\text{CH}_3^*$  desorption is included in Figure 4b for comparison. Since computational results do not rule out  $n\text{-C}_3\text{H}_7^*$  desorption from the surface, we also investigate H abstraction from enols via  $n\text{-C}_3\text{H}_7^*$ , which was found to be associated with a similar energy barrier to that with  $\text{CH}_3^*$  radicals (Figure S23) and could contribute to quenching  $n\text{-C}_3\text{H}_7^*$  by  $\text{C}_3\text{H}_8$  formation. Hydrogen abstraction from  $\text{C}_{2-3}$  enols by the resonantly stabilized  $\text{C}_3\text{H}_5^*$  involves a high-energy transition state at  $\sim 0.8$  eV (Figure S24); that is, the allyl radical is unlikely to participate in the first hydrogen transfer from enols. However, the second H-transfer step, to finally yield ketenes, is computed to be downhill, irrespective of the H-acceptor free radical. These observations imply that enols can easily dehydrogenate into ketenes in the presence of the H-acceptor radical species  $\text{CH}_3^*$ ,  $n\text{-C}_3\text{H}_7^*$ , or—as far as the second H-transfer step is concerned— $\text{C}_3\text{H}_5^*$ . However,  $n\text{-C}_3\text{H}_7^*$  radicals are also H-donor agents. In fact, a barrier-free H-transfer reaction is predicted once an  $n\text{-C}_3\text{H}_7^*$  radical collides with  $\text{CH}_3^*$ ,  $\text{C}_3\text{H}_5^*$ , or another  $n\text{-C}_3\text{H}_7^*$  associated with the release of 2 to 3 eV of energy (Figure S25), contributing to rapid quenching of  $n\text{-C}_3\text{H}_7^*$  by H loss to  $\text{C}_3\text{H}_6$  and the associated formation of  $\text{CH}_4$ ,  $\text{C}_3\text{H}_6$ , or  $\text{C}_3\text{H}_8$ . At a 0.3 bar reactor pressure, the gas-phase collision frequency is on the order of  $10^8 \text{ s}^{-1}$  at 600 °C, which implies prompt quenching of the  $n\text{-C}_3\text{H}_7^*$  radical in the presence of H acceptors. Therefore, the absence of  $n\text{-C}_3\text{H}_7^*$  radical detection can be ascribed (1) to the more favorable surface-confined  $n\text{-C}_3\text{H}_7^*$  to  $\text{C}_3\text{H}_6$  reaction path compared to  $n\text{-C}_3\text{H}_7^*$  desorption as well as (2) to its low expected lifetime in the gas phase under the reaction conditions and in the presence of H-acceptors. Since ketene and methyl radicals are both observed in the gas phase, and surface methyl and ethyl species are predicted (Figure S13), ethylketene may also be formed by the methylation of methylketene or ethylation of ketene. The formation of ethylketene is proven by *operando* PEPICO (Figure S10). Methylketene and ethylketene are known as precursors for  $\text{C}_2\text{H}_4$  and  $\text{C}_3\text{H}_6$  via decarbonylation.<sup>35</sup> However, these processes can only take place over a high barrier ( $>3$  eV) in the gas phase (Figure S26). Therefore, ketene decarbonylation is surface catalyzed and proceeds over BN to form CO and olefins, both of which desorb from the surface easily. This also explains how CO is formed in the ODHP over BN. Additionally, the detection of gas-phase oxygenates only over BN suggests they are prone to desorb from the BN surface, which also prevents deep oxidation to  $\text{CO}_2$ .

**Reaction Mechanism.** By combining *operando* PEPICO experiments and quantum chemical calculations, we have formulated a comprehensive ODHP mechanism over BN in Figure 5, involving coupled surface-confined and gas-phase reactions. Gas-phase radicals and reactive oxygenates are detected by *operando* PEPICO. Calculations predict that  $\text{C}_3\text{H}_8$  transforms into  $n\text{-C}_3\text{H}_7^*$  on the  $>\text{BO}-\text{OB}<$  site (Figure 5a),

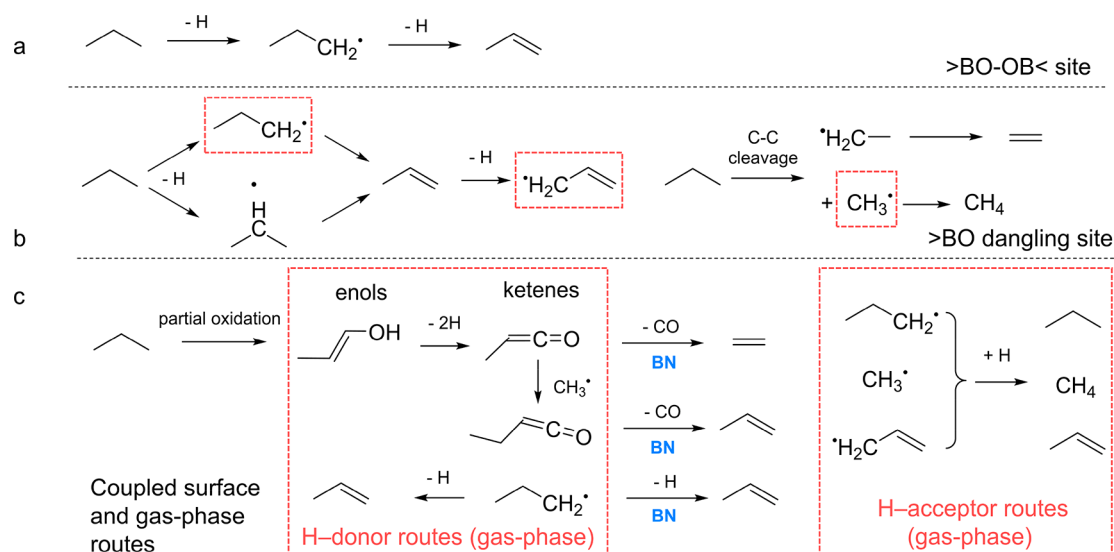


**Figure 5.** ODHP mechanism over the BN catalyst, including coupled surface-confined and gas-phase reaction routes.

which only desorbs as  $\text{C}_3\text{H}_6$  after further dehydrogenation.  $\text{C}_3\text{H}_8$  can also dissociate to  $\text{CH}_3^\bullet$  and  $\text{C}_2\text{H}_5^\bullet$ . However, both are strongly surface-bound and do not desorb from the  $>\text{BO}-\text{OB}<$  site. On the  $>\text{BO}$  dangling site,  $n\text{-C}_3\text{H}_7^\bullet$  and  $i\text{-C}_3\text{H}_7^\bullet$  are both formed after C–H activation (Figure 5b). However,  $i\text{-C}_3\text{H}_7^\bullet$  yields  $\text{C}_3\text{H}_6$  instantaneously, and only  $n\text{-C}_3\text{H}_7^\bullet$  may desorb due to its low desorption energy of 0.39 eV. Yet,  $n\text{-C}_3\text{H}_7^\bullet$  is not detected in the gas-phase experimentally, which can be attributed to the more favorable surface reaction to  $\text{C}_3\text{H}_6$  and its short gas-phase lifetime in the presence of H acceptors. Additionally,  $>\text{BO}-\text{C}_3\text{H}_6^\bullet$  can be activated to form  $\text{C}_3\text{H}_5^\bullet$  on the  $>\text{BO}$  dangling site, followed by easy desorption to form the allyl free radical. C–C cleavage on the  $>\text{BO}$  dangling site has two different reaction routes, forming  $>\text{BO}-\text{C}_2\text{H}_5^\bullet/\text{CH}_3^\bullet$  or  $>\text{BO}-\text{CH}_3^\bullet/\text{C}_2\text{H}_5^\bullet$ . The former yields gas-phase  $\text{CH}_3^\bullet$ , and the latter will transform to  $\text{C}_2\text{H}_4$ . Thus, free radicals detected by *operando* PEPICO spectroscopy are derived from the  $>\text{BO}$  dangling site. Partial oxidation products can also be observed in the gas phase with BN as a catalyst (Figure 5c). The desorption of oxygenates from the catalyst surface indicates weak bonding, which is crucial in preventing catalytic oxygenation of oxygenates into CO and  $\text{CO}_2$ .

After the desorption of radicals and oxygenates, gas-phase H-abstraction chemistry will be initiated (Figure 5c). Aside from the self-reaction to form  $\text{C}_2\text{H}_6$ , the  $\text{CH}_3^\bullet$  free radical can also abstract an H from enols. Gas-phase dehydrogenation into ketenes with H-acceptors (e.g.,  $\text{CH}_3^\bullet$ ,  $n\text{-C}_3\text{H}_7^\bullet$ , or, in the second step,  $\text{C}_3\text{H}_5^\bullet$ ) can take place readily based on G4 calculations (Figures S22–S24). Meanwhile,  $\text{CH}_3^\bullet$ ,  $n\text{-C}_3\text{H}_7^\bullet$ , and  $\text{C}_3\text{H}_5^\bullet$  will form  $\text{CH}_4$ ,  $\text{C}_3\text{H}_8$ , and  $\text{C}_3\text{H}_6$  after abstracting an H. The formed methylketene and ethylketene can then undergo surface-assisted decarbonylation to form  $\text{C}_2\text{H}_4$  and  $\text{C}_3\text{H}_6$  (Figure 5c). This new  $\text{C}_3\text{H}_6$  and  $\text{C}_2\text{H}_4$  formation mechanism is driven by methyl- and ethylketene in BN-catalyzed ODHP, which is observed for the first time. In addition to surface-bound propyl radicals ( $\text{C}_3\text{H}_7^\bullet$ ) previously considered to be the only intermediate in  $\text{C}_3\text{H}_6$  formation, this establishes partially surface-oxidized oxygenates such as  $\text{C}_3$  enols (propen-1-ol,  $\text{C}_3\text{H}_6\text{O}$ ) as precursors to  $\text{C}_3\text{H}_6$  via a gas-phase reaction sequence including dehydrogenation, methylation, and subsequent surface-confined ethylketene decarbonylation over the BN catalyst (Figure 5c).  $\text{C}_4\text{H}_8$ , only observed

over a BN catalyst, can be ascribed to the gas-phase  $\text{CH}_3^\bullet + \text{C}_3\text{H}_5^\bullet$  association reaction. Importantly, oxygenates desorb easily from the BN surface before deep oxidation to  $\text{CO}_2$ , and ketene decarbonylation is the main CO source over BN. This explains why carbon monoxide is the main deeply oxidized byproduct over BN with negligible  $\text{CO}_2$  formation. In contrast,  $\text{CO}_2$  is dominantly formed over vanadium-based catalysts, and no oxygenates can be observed in the gas phase, due to strong binding to the surface and rapid catalytic deep oxidation. Additionally, quantum chemical calculations indicate that  $n\text{-C}_3\text{H}_7^\bullet$  could escape from the catalyst surface. If so,  $n\text{-C}_3\text{H}_7^\bullet$  will participate in gaseous reactions with H-donor or H-acceptor species to form  $\text{C}_3\text{H}_6$  or  $\text{C}_3\text{H}_8$  (Figure 5c). In this coupled surface and gas-phase route (Figure 5c), H-acceptor radicals and H-donor oxygenates (or  $n\text{-C}_3\text{H}_7^\bullet$ ) react via fast H migration. The selectivity to CO rises with temperature (Figure 1a), which suggests a competitive advantage of the oxygenate route at high temperatures. Although CO is an undesirable ODHP product, it is still more useful than  $\text{CO}_2$ , making the transformation of  $\text{C}_3\text{H}_8$  and  $\text{O}_2$  to olefins and CO over boron-based catalysts alluring. Calculations also revealed the different role of chemistry at the  $>\text{BO}-\text{OB}<$  main and the  $>\text{BO}$  dangling sites. Such insights help tune the catalytic activity in a targeted way and may guide the rational design of boron-based catalysts with higher selectivity.

## CONCLUSIONS

In addition to propyl as the main precursor of propene, we identify a new H-acceptor radical- and H-donor oxygenate-driven propene formation route by *operando* PEPICO spectroscopy. Partially oxidized enols dehydrogenate in the presence of H-acceptor radicals to ketenes, which then transform to olefins by decarbonylation. Ethylketene is the observed precursor of propene in this route, which is unique to BN and absent over a vanadium-based catalyst. Moreover, we report that free radicals are derived solely from the  $>\text{BO}$  dangling site, as they are strongly bound at the  $>\text{BO}-\text{OB}<$  main site. These results not only help explain the ever-elusive ODHP reaction mechanism on BN but also aid to design next-generation boron-based catalysts for enhanced ODHP performance.

## ■ ASSOCIATED CONTENT

### Data Availability Statement

Data presented in the main figures of the manuscript and Supporting Information are publicly available through the repository: [10.16907/a8b0a8e7-8784-4789-847f-d21e52d4334c](https://doi.org/10.16907/a8b0a8e7-8784-4789-847f-d21e52d4334c).

### ■ Supporting Information

The Supporting Information is available free of charge at <https://pubs.acs.org/doi/10.1021/jacs.2c12970>.

The experimental methods, detailed PEPICO, and theoretical calculation data (PDF)

## ■ AUTHOR INFORMATION

### Corresponding Authors

Javier Pérez-Ramírez – Institute for Chemical and Bioengineering, Department of Chemistry and Applied Biosciences, ETH Zurich, 8093 Zurich, Switzerland; [orcid.org/0000-0002-5805-7355](https://orcid.org/0000-0002-5805-7355); Email: [jpr@chem.ethz.ch](mailto:jpr@chem.ethz.ch)

Patrick Hemberger – Paul Scherrer Institute, 5232 Villigen, Switzerland; [orcid.org/0000-0002-1251-4549](https://orcid.org/0000-0002-1251-4549); Email: [patrick.hemberger@psi.ch](mailto:patrick.hemberger@psi.ch)

Andras Bodi – Paul Scherrer Institute, 5232 Villigen, Switzerland; [orcid.org/0000-0003-2742-1051](https://orcid.org/0000-0003-2742-1051); Email: [andras.boedi@psi.ch](mailto:andras.boedi@psi.ch)

### Authors

Zihao Zhang – Paul Scherrer Institute, 5232 Villigen, Switzerland; [orcid.org/0000-0001-5106-2656](https://orcid.org/0000-0001-5106-2656)

Jinshu Tian – College of Chemical Engineering, Zhejiang University of Technology, Hangzhou 310014, China

Xiangkun Wu – Paul Scherrer Institute, 5232 Villigen, Switzerland; [orcid.org/0000-0001-8515-3302](https://orcid.org/0000-0001-8515-3302)

Ivan Surin – Institute for Chemical and Bioengineering, Department of Chemistry and Applied Biosciences, ETH Zurich, 8093 Zurich, Switzerland

Complete contact information is available at: <https://pubs.acs.org/doi/10.1021/jacs.2c12970>

### Author Contributions

The manuscript was written through contributions of all authors. All authors have given approval to the final version of the manuscript. Z.Z. and J.T. contributed equally to this paper.

### Notes

The authors declare no competing financial interest.

## ■ ACKNOWLEDGMENTS

Experiments were carried out at the VUV beamline of the Swiss Light Source of the Paul Scherrer Institute with support from the PSI CROSS project funding initiative. This publication was created as part of NCCR Catalysis (Grant No. 180544), a National Centre of Competence in Research funded by the Swiss National Science Foundation. DFT calculation was supported by the National Natural Science Foundation of China (22279115).

## ■ REFERENCES

- (1) Chen, S.; Chang, X.; Sun, G.; Zhang, T.; Xu, Y.; Wang, Y.; Pei, C.; Gong, J. Propane dehydrogenation: catalyst development, new chemistry, and emerging technologies. *Chem. Soc. Rev.* **2021**, *50*, 3315–3354.
- (2) Ryoo, R.; Kim, J.; Jo, C.; Han, S. W.; Kim, J.-C.; Park, H.; Han, J.; Shin, H. S.; Shin, J. W. Rare-earth–platinum alloy nanoparticles in mesoporous zeolite for catalysis. *Nature* **2020**, *585*, 221–224.
- (3) Jiao, F.; Li, J.; Pan, X.; Xiao, J.; Li, H.; Ma, H.; Wei, M.; Pan, Y.; Zhou, Z.; Li, M.; et al. Selective conversion of syngas to light olefins. *Science* **2016**, *351*, 1065–1068.
- (4) Carter, J. H.; Bere, T.; Pitchers, J. R.; Hewes, D. G.; Vandegehuchte, B. D.; Kiely, C. J.; Taylor, S. H.; Hutchings, G. J. Direct and oxidative dehydrogenation of propane: from catalyst design to industrial application. *Green Chem.* **2021**, *23*, 9747–9799.
- (5) Xing, F.; Nakaya, Y.; Yasumura, S.; Shimizu, K.-i.; Furukawa, S. Ternary platinum–cobalt–indium nanoalloy on ceria as a highly efficient catalyst for the oxidative dehydrogenation of propane using CO<sub>2</sub>. *Nat. Catal.* **2022**, *5*, 55–65.
- (6) Yan, W.; Sun, Q.; Yu, J. Dehydrogenation of propane marches on. *Matter* **2021**, *4*, 2642–2644.
- (7) Sattler, J. J.; Ruiz-Martinez, J.; Santillan-Jimenez, E.; Weckhuysen, B. M. Catalytic dehydrogenation of light alkanes on metals and metal oxides. *Chem. Rev.* **2014**, *114*, 10613–10653.
- (8) Zhou, H.; Yi, X.; Hui, Y.; Wang, L.; Chen, W.; Qin, Y.; Wang, M.; Ma, J.; Chu, X.; Wang, Y.; et al. Isolated boron in zeolite for oxidative dehydrogenation of propane. *Science* **2021**, *372*, 76–80.
- (9) Jiang, X.; Sharma, L.; Fung, V.; Park, S. J.; Jones, C. W.; Sumpter, B. G.; Baltrusaitis, J.; Wu, Z. Oxidative dehydrogenation of propane with soft oxidants via heterogeneous catalysis. *ACS Catal.* **2021**, *11*, 2182–2234.
- (10) Jiang, X.; Zhang, X.; Purdy, S. C.; He, Y.; Huang, Z.; You, R.; Wei, Z.; Meyer, H. M., III; Yang, J.; Pan, Y.; et al. Multiple Promotional Effects of Vanadium Oxide on Boron Nitride for Oxidative Dehydrogenation of Propane. *JACS Au* **2022**, *2*, 1096–1104.
- (11) Wang, C.; Han, Y.; Tian, M.; Li, L.; Lin, J.; Wang, X.; Zhang, T. Main-Group Catalysts with Atomically Dispersed In Sites for Highly Efficient Oxidative Dehydrogenation. *J. Am. Chem. Soc.* **2022**, *144*, 16855–16865.
- (12) Grant, J. T.; Venegas, J. M.; McDermott, W. P.; Hermans, I. Aerobic oxidations of light alkanes over solid metal oxide catalysts. *Chem. Rev.* **2018**, *118*, 2769–2815.
- (13) Sheng, J.; Yan, B.; Lu, W.-D.; Qiu, B.; Gao, X.-Q.; Wang, D.; Lu, A.-H. Oxidative dehydrogenation of light alkanes to olefins on metal-free catalysts. *Chem. Soc. Rev.* **2021**, *50*, 1438–1468.
- (14) Vajda, S.; Pellin, M. J.; Greeley, J. P.; Marshall, C. L.; Curtiss, L. A.; Ballentine, G. A.; Elam, J. W.; Catillon-Mucherie, S.; Redfern, P. C.; Mehmood, F. Subnanometre platinum clusters as highly active and selective catalysts for the oxidative dehydrogenation of propane. *Nat. Mater.* **2009**, *8*, 213–216.
- (15) Schumacher, L.; Weyel, J.; Hess, C. Unraveling the Active Vanadium Sites and Adsorbate Dynamics in VO<sub>x</sub>/CeO<sub>2</sub> Oxidation Catalysts Using Transient IR Spectroscopy. *J. Am. Chem. Soc.* **2022**, *144*, 14874–14887.
- (16) Barman, S.; Maity, N.; Bhatte, K.; Ould-Chikh, S.; Dachwald, O.; Haeflner, C.; Saih, Y.; Abou-Hamad, E.; Llorens, I.; Hazemann, J.-L.; et al. Single-site VO<sub>x</sub> moieties generated on silica by surface organometallic chemistry: A way to enhance the catalytic activity in the oxidative dehydrogenation of propane. *ACS Catal.* **2016**, *6*, 5908–5921.
- (17) Carrero, C.; Schlögl, R.; Wachs, I.; Schomaecker, R. Critical literature review of the kinetics for the oxidative dehydrogenation of propane over well-defined supported vanadium oxide catalysts. *ACS Catal.* **2014**, *4*, 3357–3380.
- (18) Penschke, C.; Paier, J.; Sauer, J. Vanadium oxide oligomers and ordered monolayers supported on CeO<sub>2</sub> (111): structure and stability studied by density functional theory. *J. Phys. Chem. C* **2018**, *122*, 9101–9110.
- (19) Zhang, J.; Liu, X.; Blume, R.; Zhang, A.; Schlögl, R.; Su, D. S. Surface-modified carbon nanotubes catalyze oxidative dehydrogenation of n-butane. *Science* **2008**, *322*, 73–77.



- (20) Gärtner, C. A.; van Veen, A. C.; Lercher, J. A. Oxidative dehydrogenation of ethane on dynamically rearranging supported chloride catalysts. *J. Am. Chem. Soc.* **2014**, *136*, 12691–12701.
- (21) Grant, J.; Carrero, C. A.; Goelll, F.; Venegas, J.; Mueller, P.; Burt, S. P.; Specht, S.; McDermott, W.; Chiericato, A.; Hermans, I. Selective oxidative dehydrogenation of propane to propene using boron nitride catalysts. *Science* **2016**, *354*, 1570–1573.
- (22) Liu, Z.; Yan, B.; Meng, S.; Liu, R.; Lu, W. D.; Sheng, J.; Yi, Y.; Lu, A. H. Plasma tuning local environment of hexagonal boron nitride for oxidative dehydrogenation of propane. *Angew. Chem., Int. Ed.* **2021**, *60*, 19691–19695.
- (23) Shi, L.; Wang, D.; Song, W.; Shao, D.; Zhang, W. P.; Lu, A. H. Edge-hydroxylated boron nitride for oxidative dehydrogenation of propane to propylene. *ChemCatChem* **2017**, *9*, 1788–1793.
- (24) Tian, J.; Li, J.; Qian, S.; Zhang, Z.; Wan, S.; Wang, S.; Lin, J.; Wang, Y. Understanding the origin of selective oxidative dehydrogenation of propane on boron-based catalysts. *Appl. Catal. A: Gen.* **2021**, *623*, 118271.
- (25) Lu, W.-D.; Wang, D.; Zhao, Z.; Song, W.; Li, W.-C.; Lu, A.-H. Supported boron oxide catalysts for selective and low-temperature oxidative dehydrogenation of propane. *ACS Catal.* **2019**, *9*, 8263–8270.
- (26) Grant, J. T.; McDermott, W. P.; Venegas, J. M.; Burt, S. P.; Micka, J.; Phivilay, S. P.; Carrero, C. A.; Hermans, I. Boron and boron-containing catalysts for the oxidative dehydrogenation of propane. *ChemCatChem* **2017**, *9*, 3623–3626.
- (27) Love, A. M.; Cendejas, M. C.; Thomas, B.; McDermott, W. P.; Uchupalanun, P.; Kruszynski, C.; Burt, S. P.; Agbi, T.; Rossini, A. J.; Hermans, I. Synthesis and characterization of silica-supported boron oxide catalysts for the oxidative dehydrogenation of propane. *J. Phys. Chem. C* **2019**, *123*, 27000–27011.
- (28) Love, A. M.; Thomas, B.; Specht, S. E.; Hanrahan, M. P.; Venegas, J. M.; Burt, S. P.; Grant, J. T.; Cendejas, M. C.; McDermott, W. P.; Rossini, A. J.; et al. Probing the transformation of boron nitride catalysts under oxidative dehydrogenation conditions. *J. Am. Chem. Soc.* **2019**, *141*, 182–190.
- (29) Yan, B.; Li, W.-C.; Lu, A.-H. Metal-free silicon boride catalyst for oxidative dehydrogenation of light alkanes to olefins with high selectivity and stability. *J. Catal.* **2019**, *369*, 296–301.
- (30) Venegas, J. M.; Hermans, I. The influence of reactor parameters on the boron nitride-catalyzed oxidative dehydrogenation of propane. *Org. Process Res. Dev.* **2018**, *22*, 1644–1652.
- (31) Venegas, J. M.; Zhang, Z.; Agbi, T. O.; McDermott, W. P.; Alexandrova, A.; Hermans, I. Why boron nitride is such a selective catalyst for the oxidative dehydrogenation of propane. *Angew. Chem., Int. Ed.* **2020**, *59*, 16527–16535.
- (32) Kraus, P.; Lindstedt, R. P. It's a gas: Oxidative dehydrogenation of propane over boron nitride catalysts. *J. Phys. Chem. C* **2021**, *125*, 5623–5634.
- (33) Venegas, J. M.; McDermott, W. P.; Hermans, I. Serendipity in catalysis research: boron-based materials for alkane oxidative dehydrogenation. *Acc. Chem. Res.* **2018**, *51*, 2556–2564.
- (34) Zhang, X.; You, R.; Wei, Z.; Jiang, X.; Yang, J.; Pan, Y.; Wu, P.; Jia, Q.; Bao, Z.; Bai, L.; et al. Radical chemistry and reaction mechanisms of propane oxidative dehydrogenation over hexagonal boron nitride catalysts. *Angew. Chem., Int. Ed.* **2020**, *59*, 8042–8046.
- (35) Wu, X.; Zhang, Z.; Pan, Z.; Zhou, X.; Bodi, A.; Hemberger, P. Ketenes in the Induction of the Methanol-to-Olefins Process. *Angew. Chem., Int. Ed.* **2022**, *61*, e202207777.
- (36) Cesarini, A.; Mitchell, S.; Zichittella, G.; Agrachev, M.; Schmid, S. P.; Jeschke, G.; Pan, Z.; Bodi, A.; Hemberger, P.; Pérez-Ramírez, J. Elucidation of radical and oxygenate-driven paths in zeolite-catalysed conversion of methanol and methyl chloride to hydrocarbons. *Nat. Catal.* **2022**, *5*, 605–614.
- (37) Tian, J.; Tan, J.; Xu, M.; Zhang, Z.; Wan, S.; Wang, S.; Lin, J.; Wang, Y. Propane oxidative dehydrogenation over highly selective hexagonal boron nitride catalysts: The role of oxidative coupling of methyl. *Sci. Adv.* **2019**, *5*, eaav8063.
- (38) Bodi, A.; Hemberger, P.; Gerber, T.; Sztáray, B. A new double imaging velocity focusing coincidence experiment:  $i^2$ PEPICO. *Rev. Sci. Instrum.* **2012**, *83*, 083105.
- (39) Sztáray, B.; Voronova, K.; Torma, K. G.; Covert, K. J.; Bodi, A.; Hemberger, P.; Gerber, T.; Osborn, D. L. CRF-PEPICO: Double velocity map imaging photoelectron photoion coincidence spectroscopy for reaction kinetics studies. *J. Chem. Phys.* **2017**, *147*, 013944.
- (40) Hemberger, P.; van Bokhoven, J. A.; Pérez-Ramírez, J.; Bodi, A. New analytical tools for advanced mechanistic studies in catalysis: photoionization and photoelectron photoion coincidence spectroscopy. *Catal. Sci. Technol.* **2020**, *10*, 1975–1990.
- (41) Hemberger, P.; Bodi, A.; Bierkandt, T.; Köhler, M.; Kaczmarski, D.; Kasper, T. Photoelectron photoion coincidence spectroscopy provides mechanistic insights in fuel synthesis and conversion. *Energy Fuels* **2021**, *35*, 16265–16302.
- (42) Chowdhury, A. D.; Gascon, J. The curious case of ketene in zeolite chemistry and catalysis. *Angew. Chem., Int. Ed.* **2018**, *57*, 14982–14985.
- (43) Mansur, A. R.; Nam, T. G.; Jang, H. W.; Cho, Y.-S.; Yoo, M.; Seo, D.; Ha, J. Determination of 2-propanol using headspace solid-phase microextraction coupled to gas chromatography–time-of-flight mass spectrometry as a marker for authentication of unrefined sesame oil. *J. Chem.* **2017**, *2017*, 1.
- (44) Taatjes, C. A.; Hansen, N.; McIlroy, A.; Miller, J. A.; Senosiain, J. P.; Klippenstein, S. J.; Qi, F.; Sheng, L.; Zhang, Y.; Cool, T. A.; et al. Enols are common intermediates in hydrocarbon oxidation. *Science* **2005**, *308*, 1887–1889.
- (45) Ruscic, B.; Pinzon, R. E.; Von Laszewski, G.; Kodeboyina, D.; Burcat, A.; Leahy, D.; Montoy, D.; Wagner, A. F. Active Thermochemical Tables: thermochemistry for the 21st century. In *J. Phys. Conf. Ser. Vol. 16*; IOP Publishing, 2005; p 078.
- (46) Li, Y.; Zhang, X.; He, H.; Yu, Y.; Yuan, T.; Tian, Z.; Wang, J.; Li, Y. Effect of the pressure on the catalytic oxidation of volatile organic compounds over Ag/Al<sub>2</sub>O<sub>3</sub> catalyst. *Appl. Catal. B: Environ.* **2009**, *89*, 659–664.
- (47) Zhang, Y.; Gao, P.; Jiao, F.; Chen, Y.; Ding, Y.; Hou, G.; Pan, X.; Bao, X. Chemistry of Ketene Transformation to Gasoline Catalyzed by H-SAPO-11. *J. Am. Chem. Soc.* **2022**, *144*, 18251–18258.
- (48) Jiao, F.; Pan, X.; Gong, K.; Chen, Y.; Li, G.; Bao, X. Shape-Selective Zeolites Promote Ethylene Formation from Syngas via a Ketene Intermediate. *Angew. Chem., Int. Ed.* **2018**, *57*, 4692–4696.
- (49) Fu, H.; Liu, Z. P.; Li, Z. H.; Wang, W. N.; Fan, K. N. Periodic density functional theory study of propane oxidative dehydrogenation over V<sub>2</sub>O<sub>5</sub> (001) surface. *J. Am. Chem. Soc.* **2006**, *128*, 11114–11123.
- (50) Gilardoni, F.; Bell, A. T.; Chakraborty, A.; Boulet, P. Density functional theory calculations of the oxidative dehydrogenation of propane on the (010) surface of V<sub>2</sub>O<sub>5</sub>. *J. Phys. Chem. B* **2000**, *104*, 12250–12255.
- (51) Rozanska, X.; Fortrie, R.; Sauer, J. Oxidative dehydrogenation of propane by monomeric vanadium oxide sites on silica support. *J. Phys. Chem. C* **2007**, *111*, 6041–6050.
- (52) Alarcon, J. F.; Ajo, S.; Morozov, A. N.; Mebel, A. M. Theoretical study on the mechanism and kinetics of the oxidation of allyl radical with atomic and molecular oxygen. *Combust. Flame* **2022**, 112388.